Enhanced wave localization in multifractal scattering media

Y. Chen,[1] F. Sgrignuoli,[2] Y. Zhu,[3] T. Shubitidze,[1] and L. Dal Negro[1,3,4,*]

[1]*Department of Electrical and Computer Engineering & Photonics Center, Boston University, 8 Saint Mary's Street, Boston, Massachusetts 02215, USA*

[2]*Institute of Applied Sciences and Intelligent Systems, National Research Council, Via Pietro Castellino, Naples 80131, Italy*

[3]*Division of Materials Science & Engineering, Boston University, 15 Saint Mary's St. Brookline, Massachusetts 02446, USA*

[4]*Department of Physics, Boston University, 590 Commonwealth Avenue, Boston, Massachusetts 02215, USA*

(Received 30 August 2022; revised 18 November 2022; accepted 23 January 2023; published 2 February 2023)

In this paper, we study the structural, scattering, and wave localization properties of multifractal arrays of electric point dipoles generated from multiplicative random fields with different spectra of fractal dimensions. Specifically, using the rigorous Green's matrix method, we investigate the scattering resonances and wave localization behavior of systems with $N = 10^4$ dipoles and demonstrate an enhanced localization behavior in highly inhomogeneous multifractal structures compared to homogeneous fractals, or monofractals. We show distinctive spectral properties, such as the absence of level repulsion in the strong multiple scattering regime and power-law statistics of level spacings, which indicate a clear localization transition enhanced in nonhomogeneous multifractals. Our findings unveil the importance of multifractal structural correlations in the multiple scattering regime of electric dipole arrays and provide an efficient model for the design of multiscale nanophotonic systems with enhanced light-matter coupling and localization phenomena beyond what is possible with traditional fractal systems.

DOI: 10.1103/PhysRevB.107.054201

I. INTRODUCTION

In recent years, self-similar structures have attracted significant interest in photonics and nano-optics technologies [1–4], adding unique functionalities to the manipulation of optical fields in complex media [5–7] beyond periodic [8] or disordered systems [9,10], with applications to resonant nanodevices and metamaterials [11–13]. Statistically homogeneous optical media with fractal geometries, which naturally occur in a wide variety of physical systems, including colloidal aggregates [14] and certain emulsions [15], motivated earlier studies on the single scattering properties of light in self-similar structures [16]. Recently, the light transport through fractal structures beyond the single scattering regime has also been studied, leading to the demonstration of photon superdiffusive phenomena in Lévy glass optical media [17,18]. These are unique homogeneous materials containing TiO_2 nanoparticles and engineered fractal distributions of polydispersed glass spheres that enable control of photon scattering events in a self-similar environment with a small refractive index contrast. However, the complex geometry of many physical structures and multiscale phenomena, ranging from fully developed turbulence and weather systems to the clustering of galaxies, network traffic, and the stock market, display very irregular fluctuations that cannot be adequately described by simple homogeneous fractal models. Starting from the pioneering work of Hentschel and Procaccia, multifractal systems have been characterized by a distribution of fractal scaling exponents D_q, where q often is not an integer [19]. In particular, Halsey *et al.* proposed the continuum spectrum of fractal scaling exponents $f(\alpha)$, also known as the singularity spectrum, which is frequently used for the characterization of multifractal structures [20]. These ideas led to the rigorous theory of multifractality [21–25] which, originally introduced to analyze multiscale energy dissipation in turbulent flows [25,26], significantly broadened our understanding of complex structures in science and engineering [27–32]. Critical phenomena in disordered quantum and classical systems have been the subject of intense theoretical and experimental research, leading to the discovery of multifractality in electronic and optical wave functions at the metal-insulator Anderson transition for conductors [33–36], superconductors [37], atomic matter waves [38], and engineered nanophotonic structures [39–43]. Besides its fundamental interest, understanding the behavior of optical waves in strongly scattering multifractal media could offer a mechanism to localize and resonantly distribute classical and quantum light states at multiple length scales and to enhance light-matter coupling across broad frequency spectra. However, to the best of our knowledge, the distinctive multiple scattering and localization behavior of optical waves in multifractal arrays with controlled spectra of scaling exponents is still missing.

In this paper, we use the rigorous Green's matrix spectral method that enables a systematic investigation of complex scattering resonances and their spectral statistics to investigate the localization properties of light in open two-dimensional scattering arrays of electric dipoles (i.e., systems with in-plane radiation losses) with fractal and multifractal geometrical arrangements. Specifically, by studying the Thouless conductance g [44] and the first-neighbor level

*dalnegro@bu.edu

spacing statistical distribution for different values of the optical density, our work demonstrates clear signatures of a broadband localization transition with significantly reduced g values in multifractals compared to their monofractal counterparts. Moreover, we discover that multifractal arrays support a significantly larger density of eigenmodes in the localization regime. Finally, we demonstrate a crossover in the spectral statistics of level spacing from a level repulsion behavior, described by the Gaussian unitary ensemble (GUE) of random matrices [45] at low optical density, to a level clustering behavior with power-law level spacing distributions at large optical density. Our findings show enhanced localization properties in highly inhomogeneous multifractal arrays compared to traditional fractal systems and provide yet-unexplored possibilities to systematically exploit multifractality as a strategy for the engineering of nanophotonic systems and metamaterials with broadband localization properties for optical sensing, random lasing, and multispectral devices.

Our paper is organized as follows. In Sec. II, we introduce background concepts on fractals and multifractals. In Sec. III, we discuss the generation of the investigated fractal and multifractal arrays and introduce their structural and wave diffraction properties. In Sec. IV, we present our results on the spectral and localization properties of the scattering resonances of fractals and multifractals, and we draw our conclusions in Sec. V. Finally, in Appendix A we review the relevant concepts of multifractal analysis and in Appendix B we summarize the single scattering (i.e., diffraction) properties of fractals and multifractals.

II. FRACTALS AND MULTIFRACTALS

Fractal objects are characterized by noninteger fractal dimensions and exhibit power-law scaling of structural (i.e., density-density correlation, structure factor) and dynamical (i.e., density of modes, spectral functions) properties [46]. In fractal systems, the exponent of the power-law scaling of the mass with the system size does not coincide with the Euclidean dimension. This property implies very large local density fluctuations and high lacunarity [46], leading to the existence of both very dense and very empty regions. The fractal dimensions of physical objects is operationally defined using the box-counting method [47]. In this approach, the space embedding the fractal is subdivided into a hypercubic grid of boxes (i.e., cells) of linear size ϵ (i.e., line segments in the case of one-dimensional objects, squares in two dimensions, cubes in three dimensions, and so on). For a given box of size ϵ, the minimum number of boxes $N(\epsilon)$ needed to cover all the points of the object is determined and this procedure is repeated for several box sizes. Finally, the (box-counting) fractal dimension D_0 is obtained from the power-law scaling:

$$N(\epsilon) \propto \epsilon^{-D_0}. \tag{1}$$

The procedure can be extended to any suitable measure defined on a set, and the fractal properties of the measure (e.g., the number of components or the mass density of an object) are deduced by studying the scaling behavior of its moments with respect to the size of covering partitions of the set. Alternatively, for arrays of point particles we can determine the fractal dimension by drawing a sphere of radius r and computing the total number (or the mass) of the particles included in this sphere, denoted by $N(r)$. Moreover, if randomness is involved in the fractal object, we then consider the scaling of $N(r)$ over spheres with different centers and the (average) fractal dimension D_m follows from the scaling law:

$$\langle N(r) \rangle \propto r^{D_m}. \tag{2}$$

Here $\langle \ldots \rangle$ denotes the average over different spheres with radius r and the fractal dimension D_m is also called the mass fractal dimension [46]. The box-counting or mass fractal dimension introduced above provides a concise description of how the size or mass of a fractal varies with respect to the magnification scale ϵ. Objects that are uniquely described by a constant (scale-independent) fractal dimension are called homogeneous fractals, or monofractals, and possess features that repeat identically at every scale, i.e., they exhibit scale-invariance symmetry or self-similarity over a large range of scales. The relevance of fractals to physical sciences and other disciplines (i.e., economics) was originally pointed out by the pioneering work of Mandelbrot [48]. More recently, the concept of multifractals, or inhomogeneous fractals, has been introduced to characterize complex systems with space or time-dependent self-similar properties and a rigorous multifractal formalism has been developed to quantitatively describe their local scaling [22,25,26], which is briefly reviewed in Appendix A.

Examples of multifractal structures and phenomena are commonly encountered in dynamical systems theory (e.g., strange attractors of nonlinear maps), physics (e.g., diffusion-limited aggregates, fluid dynamics), engineering (e.g., random resistive networks, image analysis), geophysics (e.g., rock shapes, creeks), and atmospheric science (analysis of rain and clouds), as well as in statistics and finance (e.g., extreme value theory, stock markets fluctuations) [22,25,28,29,47,49]. Generally, when dealing with multifractals on which a local measure μ is defined (i.e., a mass density, a velocity component, an electrical signal, or some other scalar physical parameter defined on the fractal object), the (local) singularity strength $\alpha(x)$ of the multifractal measure μ obeys the more complex scaling law [27]

$$\mu[B_x(\epsilon)] \propto \epsilon^{\alpha(x)}, \tag{3}$$

where $B_x(\epsilon)$ denotes a ball (i.e., an open interval) of small radius ϵ centered at x. The exponent $\alpha(x)$ measures the local singularity of the measure, i.e., the smaller the exponent $\alpha(x)$, the more singular the measure around x. The multifractal spectrum $f(\alpha)$, also known as the singularity spectrum, characterizes the statistical distribution of the singularity exponent $\alpha(x)$ of the multifractal measure [47,49]. Moreover, if we cover the support of the measure μ with balls of size ϵ, the number of balls $N_\alpha(\epsilon)$ which, for a given α, scales like ϵ^α, is given by [27]

$$N_\alpha(\epsilon) \propto \epsilon^{-f(\alpha)}. \tag{4}$$

It has been established that in the limit of vanishingly small ϵ, $f(\alpha)$ coincides with the fractal dimension of the set of all points x with the same scaling index α. The spectrum $f(\alpha)$ was originally introduced by Frisch and Parisi [25] to investigate the energy dissipation of turbulent fluids. From a

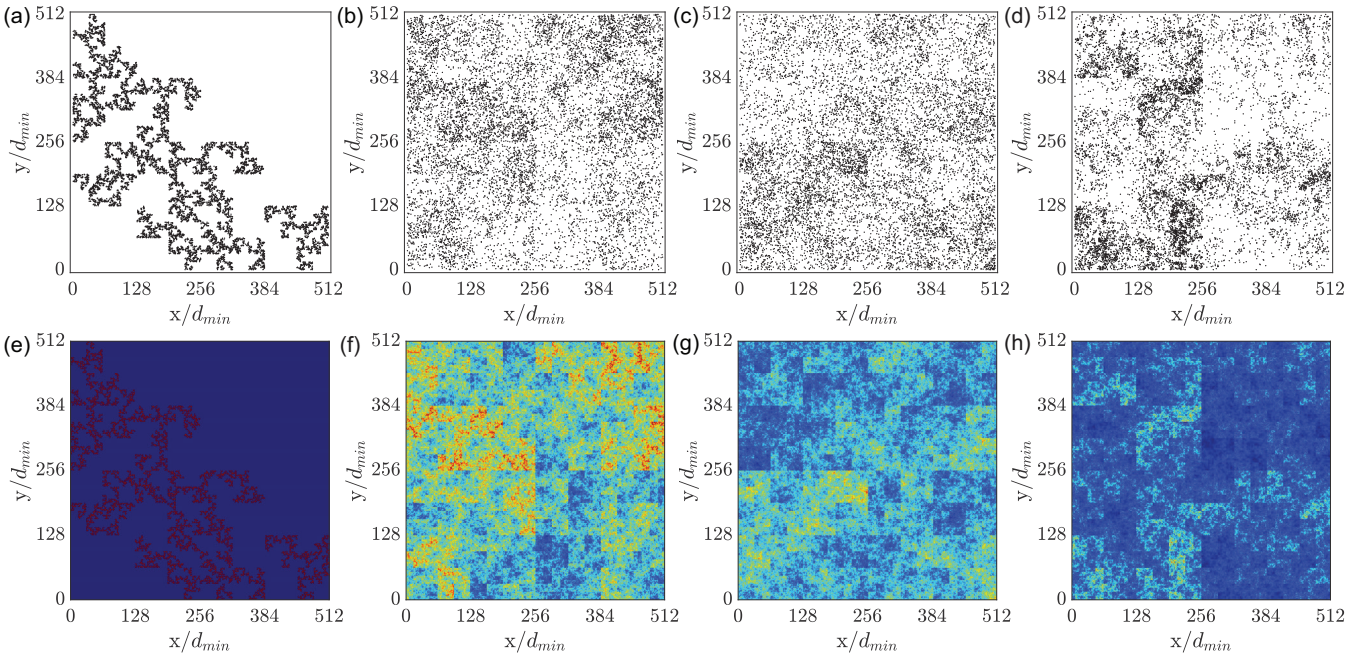

FIG. 1. (a)–(d) Point patterns and (e)–(h) probability matrices for single realization multifractal structures. (a), (e); (b), (f); (c), (g); and (d), (h) refer to the single realization of multifractal patterns composed by 10 000 elements and generated with probabilities $p = [1, 1, 1, 0]$, $p = [1, 1, 0.75, 0.5]$, $p = [1, 0.75, 0.75, 0.5]$, $p = [1, 0.75, 0.5, 0.25]$, respectively.

physical point of view, the multifractal spectrum is a quantitative measure of structural inhomogeneity and is well suited for characterizing complex spatial signals because it can efficiently resolve their local fluctuations. In the case of multifractal measures with a recursive multiplicative structure, such as the ones investigated in this paper, the multifractal spectrum can be calculated analytically [50]. However, in general, it is obtained numerically by implementing the formalism reviewed in Appendix A using, for example, the efficient approach developed by Chhabra and Jensen [24].

III. MULTIFRACTAL ARRAYS

Multifractal structures were originally proposed to study turbulent flows and chaotic dynamical systems, where they originate from nonlinear mechanisms [25,26,51]. However, in the context of wave scattering and diffraction physics, simpler and nongeneric multifractals with analytical spectra are often constructed using random multiplicative cascade processes to investigate complex media [52]. Moreover, simple multiplicative processes are also utilized to describe complex structures that appear in a variety of fields from atmospheric turbulence, astrophysics, and in the study of porous media [22,50,52–55]. The multifractal scattering arrays investigated in this paper are generated using random multiplicative cascades. A random multiplicative cascade model [52] is constructed by first dividing a square into four equal squares. To each of the subsquares, one assigns the probabilities $p_i \in [0, 1]$, with $i = 1, 2, 3, 4$. This constitutes the first iteration of the process ($n = 1$). At the second iteration ($n = 2$), each of the four subsquares is further divided in four squares, and the probabilities associated with each subdivision are multiplied in random order with the ones of the previous iterations. At the third iteration, one performs a similar division into subsquares and to each of them assigns the probabilities in random permutations from the previous iterations, i.e., $n = 1$ and $n = 2$. The resulting multiplicative cascade multifractal distribution is the probability field obtained in the limit of a large number of iterations [50]. The probability value attached to a square region is the product of the p_i's of the square and all its ancestors at previous generations and the distribution of cell values strictly depends on the initial choice of the probability vector p_i. Because the random numbers in the probability fields are generated multiplicatively, the corresponding process is a multiplicative random process that is generally non-Gaussian. Random point patterns (i.e., point processes) with multifractal scaling properties induced by the probability fields introduced above are generated by distributing N particles on the underlying square lattice with probabilities that are simply proportional to the square-cell values. We used a Monte Carlo rejection scheme for generating multifractal arrays with $N = 10^4$ point dipoles [50].

In Fig. 1, we show the investigated arrays in panels (a)–(d) and the corresponding probability fields in panels (e)–(h). The arrays are constructed from the four probability vectors reported in the caption. These are chosen so the array in Fig. 1(a) is a statistically homogeneous fractal while the arrays in Figs. 1(b)–1(d) are multifractals with an increasing degree of spatial nonuniformity and structural properties intermediate between uncorrelated random point patterns and monofractal ones. All the length scales in Fig. 1 are normalized with respect to the minimum interparticle separation $d_{\min} = 1\,\mu$m. The multifractal spectra of the considered particle arrays are computed analytically in the limit of systems with large size L. In particular, the spectrum of generalized dimensions has the following expression [50]:

$$D_q = \frac{1}{1-q}\log_2\left(f_1^q + f_2^q + f_3^q + f_4^q\right), \tag{5}$$

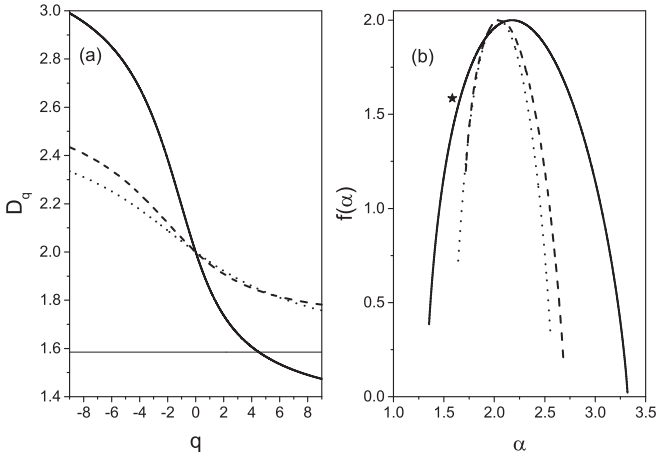

FIG. 2. (a) Spectra of generalized dimensions D_q and (b) multifractal singularity spectra $f(\alpha)$ for multifractal structures generated with probability vectors $p = [1, 1, 1, 0]$ (thin solid line and star symbol), $p = [1, 1, 0.75, 0.5]$ (dotted line), $p = [1, 0.75, 0.75, 0.5]$ (dashed line), and $p = [1, 0.75, 0.5, 0.25]$ (thick solid line).

where $f_i = p_i / \sum_{i=1}^{4} p_i$ with $i = 1, 2, 3, 4$. The corresponding multifractal spectrum $f(\alpha)$ is then calculated according to Eq. (A7), where $\tau(q) = (1 - q)D_q$. The spectra of generalized dimensions D_q and the multifractal spectra $f(\alpha)$ for the investigated arrays shown in Fig. 1 are displayed in Fig. 2. The results show clearly a transition from a homogeneous fractal structure, featuring a constant box-counting $D_0 \approx 1.58$ with $f(\alpha)$ supported only by a single point, to more inhomogeneous multifractals characterized by increasingly broader $f(\alpha)$ spectra for decreasing amplitudes of the initial probability vectors.

In Fig. 3, we further characterize the geometrical structure of the investigated arrays by analyzing the normalized probability distributions of the first-neighbor distances of

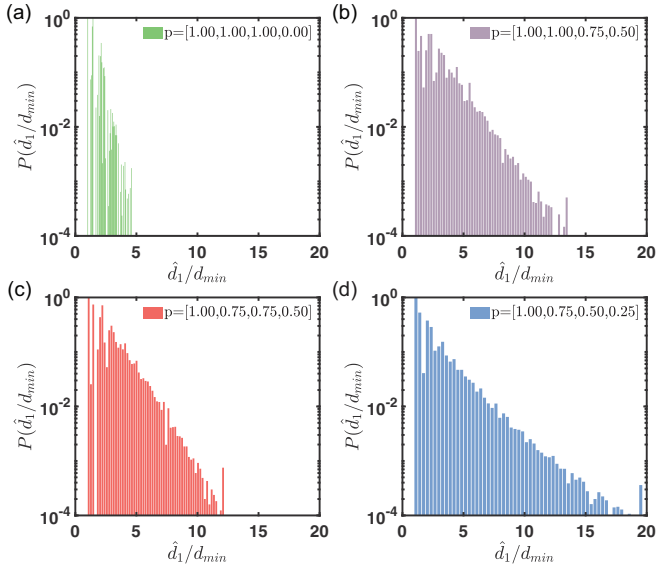

FIG. 3. Normalized histograms of first-neighbor distances for multifractal structures generated with probabilities (a) $p = [1, 1, 1, 0]$, $p = [1, 1, 0.75, 0.5]$, $p = [1, 0.75, 0.75, 0.5]$, $p = [1, 0.75, 0.5, 0.25]$.

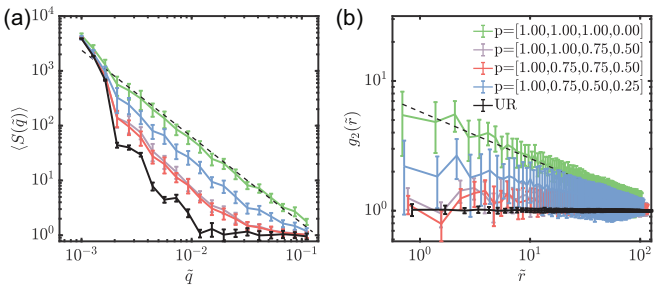

FIG. 4. (a) Azimuthally averaged structure factor $\langle S(\tilde{q}) \rangle$, where $\tilde{q} = q/q_{max}$, and (b) radial distribution function $g_2(\tilde{r})$, which gives the probability of finding two particles separated by a normalized distance $\tilde{r} = r/d_{min}$, over 25 realizations for multifractal structures generated with the probability vectors specified in the legend and the uniform random patterns. Both panels share the same legend.

the particles averaged over 25 realizations of the disorder. Our findings show that multifractal arrays have significantly broader probability distributions compared to the monofractal case shown in Fig. 3(a), consistently with the increased degree of spatial nonuniformity associated to their broader multifractal spectra. Specifically, we found that the arrays with the broader support of the spectrum $f(\alpha)$ also feature the larger range of distances in the distribution histograms shown in Fig. 3.

In Fig. 4, we address the single scattering wave properties of the analyzed fractal and multifractal structures by showing in panel (a) the azimuthally averaged structure factors. In the plot, the radial wave number q has been normalized with respect to the maximum wave number $q_{max} = 1\,\mu m^{-1}$. As a comparison, we also report the results obtained on uniform random structures (URs) with the same density and averaged over 25 different realizations. We notice that the averaged structure factor of the URs deviates from unity close to the origin of the q space due to the finite size of the patterns that we have investigated. Therefore, to accurately characterize the structural properties of all the investigated systems, we also computed their radial distribution functions, which are shown in Fig. 4(b). We note that the correlation distance $\hat{d}_1$ has been normalized with respect to the minimum interparticle separation d_{min}. It is well-known that for fractals and multifractals, these quantities display a power-law decay with a slope determined by the average fractal dimension [56,57] (see Appendix B). In particular, for a homogeneous fractal, the pair-correlation scales as $g_2(r) \propto r^{-\beta}$ and similarly for the structure factor $S(q) \propto |q|^{-(d-\beta)}$, where $0 < \beta < d$, consistently with the data presented in Fig. 4. In particular, for the monofractal structure (green lines) the slopes extracted from the linear fit of the structure factor and the $g_2(r)$ in double logarithmic scale yield exactly the box-counting fractal dimension $D_0 = 1.58$ with $\beta = d - D_0$. However, the exact relation between the exponent β and the fractal dimension D_0 is nontrivial for more general fractals and multifractals, as it depends on the process of structure formation as well as their spatial distributions [58]. In all cases, it is important to realize that realistic finite-size systems exhibit lower and upper bound cutoffs in their fractal or multifractal nature. This implies that the power-law decays are observed only over a small range of

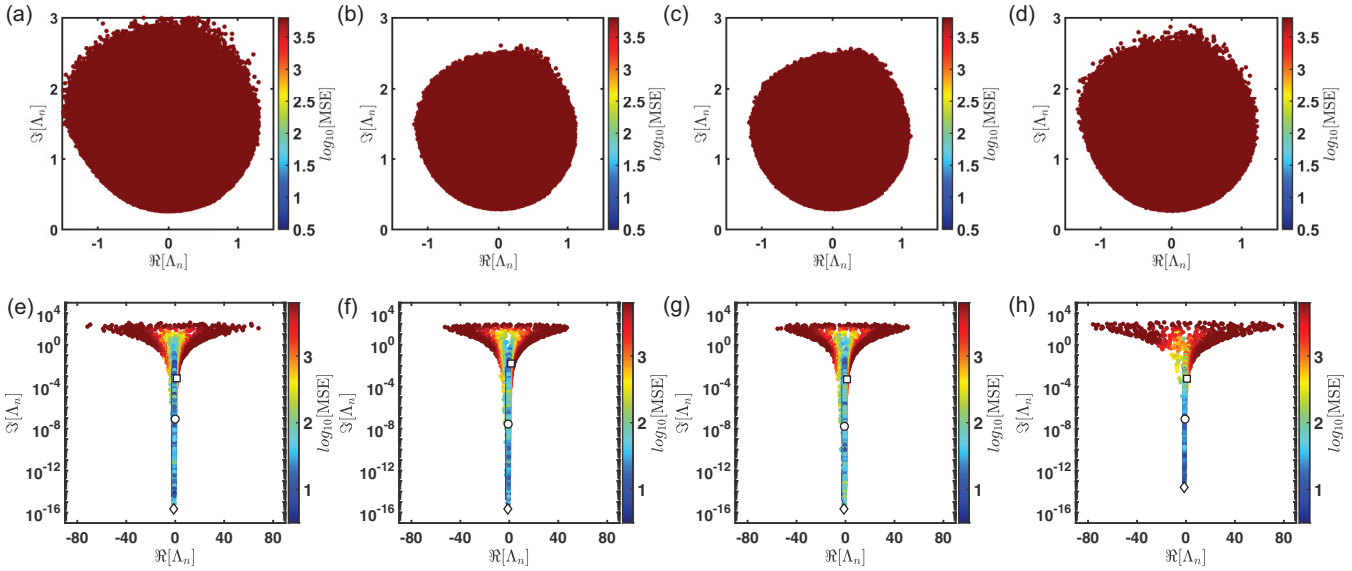

FIG. 5. (a)–(h) The complex eigenvalue distribution, color coded with respect to the MSE parameter, of 25 different realizations of the point patterns presented in Fig. 1. Specifically, (a)–(d) and (e)–(h) refer to two different optical regimes characterized by a value of $\rho\lambda^2$ equal to 10^{-6} and 50, respectively. The different markers in the (e)–(h) identify the spectral positions of the representative scattering resonances reported in Fig. 5.

scales and the correlation $g_2(r)$ eventually converges to 1 at large r, as shown in Fig. 4(b). Moreover, Fig. 4 shows how the selected arrays display structural properties that interpolate in between homogeneous fractals and uncorrelated random media, offering a representative overview of the behavior of scalar waves in these large-scale complex systems. We provide additional information on the single scattering properties of fractals and multifractals in Appendix B and focus next on the multiple scattering regime.

IV. SPECTRAL AND LOCALIZATION PROPERTIES OF MULTIFRACTAL ARRAYS

We now investigate the wave transport and localization properties of TM-polarized electric dipoles that are spatially arranged as in Fig. 1. Multiple scattering effects in two spatial dimensions (i.e., for cylindrical waves) are studied by analyzing the spectral properties of the Green s matrix defined as

$$G_{ij} = i(\delta_{ij} + \tilde{G}_{ij}), \tag{6}$$

where the elements $\tilde{G}_{ij}$ are given by [59]

$$\tilde{G}_{ij} = \frac{2}{i\pi} K_0(-ik_0|\mathbf{r}_i - \mathbf{r}_j|), \tag{7}$$

and $K_0(-ik_0|\mathbf{r}_i - \mathbf{r}_j|)$ denotes the modified Bessel function of the second kind, k_0 is the wave vector of light, and $\mathbf{r}_i$ specifies the position of the ith scattering dipole in the array. The non-Hermitian matrix Eq. (6) describes the electromagnetic coupling among the scatterers and the real and imaginary part of its complex eigenvalues Λ_n ($n \in 1, 2, \cdots N$) correspond to the detuned frequency ($\omega_0 - \omega$) and decay rate Γ_n (both normalized to the resonant width Γ_0 of an isolated dipole) of the scattering resonances of the system [59,60]. This formalism accounts for all the multiple scattering orders and enables the systematic study of the scattering properties of 2D waves with an electric field parallel to the invariance axis of the scatterers [61]. Even though the 2D model in Eq. (6) does not take into account the vector nature of light [62,63], it still provides useful information on the localization properties of light in 2D disorder media [59] and aperiodic structures [64], and transparency in high-density hyperuniform materials [61]. Moreover, it correctly describes the coupling between one or several quantum emitters embedded in structured dielectric environments [42,65,66].

To investigate the spectral properties of the designed arrays, we analyze the distributions of the complex eigenvalues and representative scattering resonances, the behavior of the Thouless number g as a function of the frequency ω, and study its minimum value for each considered optical density $\rho\lambda^2$, as well as the level spacing statistics for different values of $\rho\lambda^2$. Here, ρ denotes the number of scatterers per the unit area and λ is the optical wavelength. The spectral information is derived by numerically diagonalizing the $N \times N$ Green's matrix Eq. (7).

At low optical density (i.e., $\rho\lambda^2 = 10^{-6}$), all the investigated systems are in the diffusive regime. Accordingly, their eigenvalue distributions, color-coded according to $\log_{10}$ of the modal spatial extent (MSE), do not show the formation of any long-lived scattering resonances, as shown in Figs. (5)(a)–5(d). The MSE parameter quantifies the spatial extension of a given scattering resonances Ψ_i of the system and it is defined as [67]

$$\mathrm{MSE} = \left(\sum_{i=1}^{N} |\Psi_i|^2\right)^2 \Big/ \sum_{i=1}^{N} |\Psi_i|^4. \tag{8}$$

On the other hand, at large optical density $\rho\lambda^2 = 50$, we observe the appearance of long-lived scattering resonances forming near $\omega \approx -2$, as visible in Figs. 5(e)–5(h). Con-

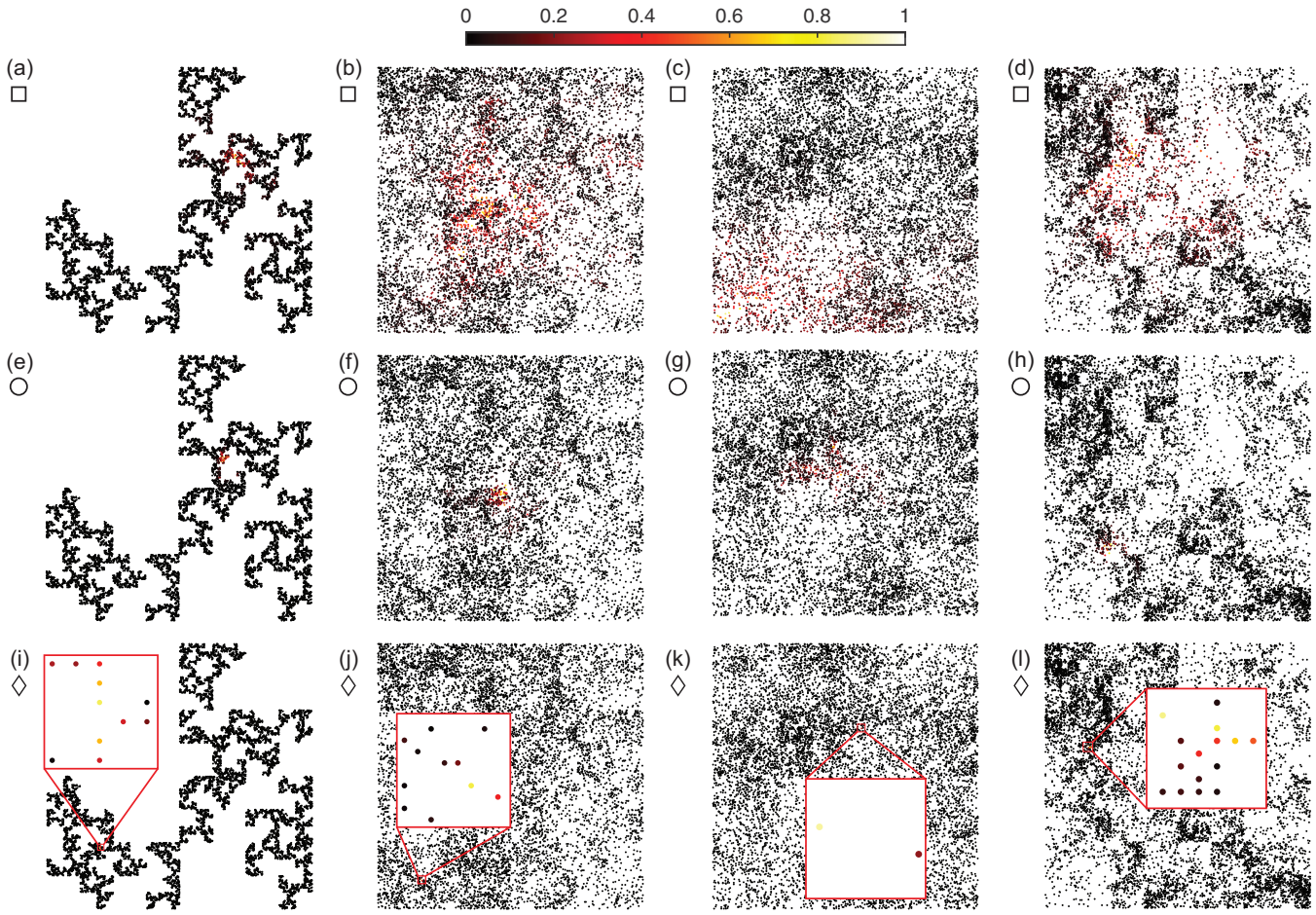

FIG. 6. Representative scattering resonances of the investigated structures in the multiple scattering regime. While (a), (e), (i) refer to the monofractal point pattern generated with a probability $p = [1, 1, 1, 0]$, (b), (f), (j); (c), (g), (k); and (d), (h), (l) display critical and Efimov-type few-body scattering resonances characterizing multifractal point patterns when p is equal to [1,1,0.75,0.5], [1,0.75,0.75,0.5], and [1,0.75,0.5,0.25], respectively. The point pattern length scales are the same as shown in Fig. 1.

sistently, the corresponding Green s matrix eigenvectors, reported in Fig. 6, are spatially localized over small clusters of dipoles demonstrating the formation of Efimov-type few-body scattering resonances occurring due to locally symmetric particle clusters distributed across the investigated structures [62,68]. Moreover, Fig. 5 also shows the formation of critical scattering resonances for point patterns with multifractal properties. Critical modes are spatially extended and long-lived resonances with spatial fluctuations at multiple length scales characterized by a power-law scaling behavior [69,70], which are the results of the effect of local correlations on wave interference across the structures [41].

The Thouless number g as a function of ω is evaluated as

$$g(\omega) = \frac{\overline{\delta\omega}}{\overline{\Delta\omega}} = \frac{\overline{(1/\mathrm{Im}[\Lambda_n])}^{-1}}{\overline{\mathrm{Re}[\Lambda_n] - \mathrm{Re}[\Lambda_{n-1}]}}, \tag{9}$$

following the same procedure as in our previous work [62,64,68,71]. In particular, we have sampled the real parts of the eigenvalues of the Green s matrix in 5000 equispaced intervals and we computed Eq. (9) in each frequency subinterval. The symbol $\overline{\{\cdots\}}$ in Eq. (9) denotes the subinterval averaging operation, while ω indicates the central frequency of each subinterval. We have verified that the utilized frequency sampling resolution does not affect the presented results.

Figure 7 shows the results of the Thouless number analysis in both the dilute and multiple scattering regimes. Consistently with the low value of the optical density, we found that the Thouless number is always larger than the one, indicating a diffusive regime [63,64]. At larger optical density, the Thouless number shows a completely different behavior with clear spectral ranges where g drops below one, indicating the onset of light localization. We remark that the long-lived scattering resonances that are spatially confined over a few scatterers appear at the frequency positions where the Thouless number becomes lower than one. Interestingly, we found that point patterns with multifractal geometrical feature-enhanced localization effects characterized by significantly smaller Thouless numbers compared to the investigated monofractal structures generated with a probability p equal to [1, 1, 1, 0] (i.e., pastel green markers). This outcome is more evident by looking at the insets in Figs. 7(e)–7(h), showing an enlarged view of the Thouless number in the frequency range $\omega \in [-10, 2]$.

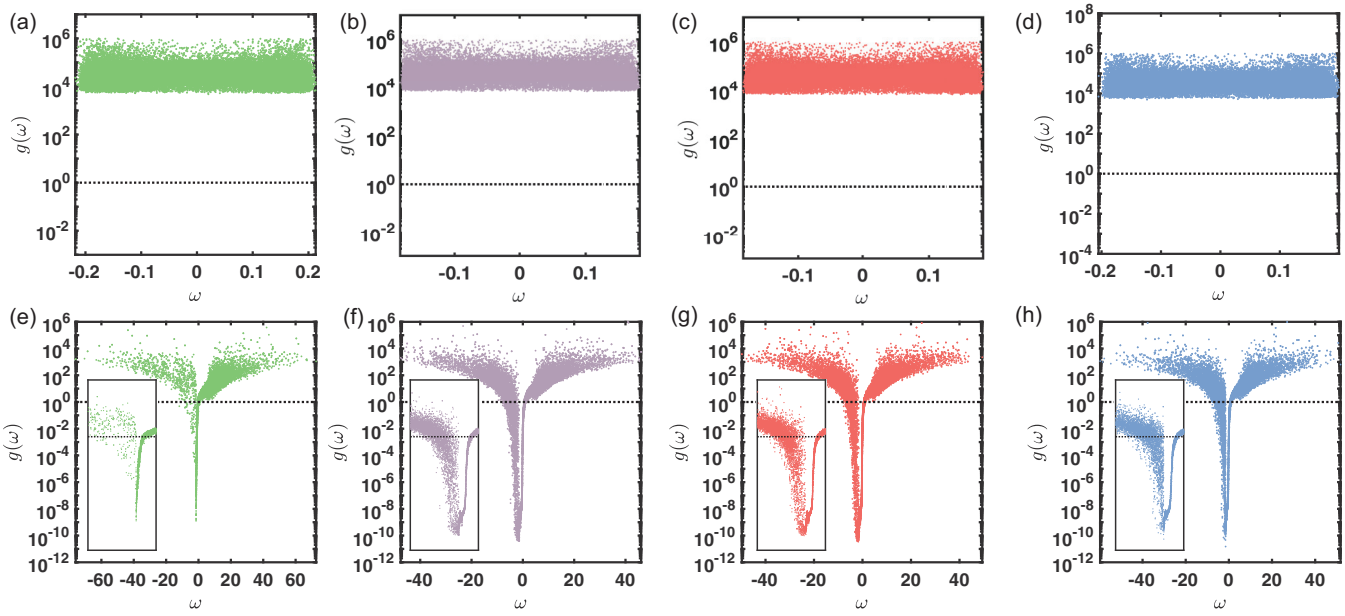

FIG. 7. (a)–(d) and (e)–(h) Thouless number as a function of the frequency ω extrapolated from the distribution reported in Figs. 4(a)–4(d) and 4(e)–4(h), respectively. The pastel green, violet, red, and blue dots correspond to the Thouless number of 25 different disorder realizations produced when $\rho\lambda^2$ is equal to 10^{-6} [i.e., (a)–(d)] and to 50 [i.e., (e)–(h)], respectively. The dashed-black lines identify the threshold of the diffusion-localization transition. (e)–(h) Zoom-in view in the range $\omega \in [-10, 2]$.

To obtain additional insights on the localization behavior of multifractal structures, we analyze the minimum value of the Thouless number as a function of $\rho\lambda^2$. Specifically, we have evaluated $g = g(\omega)$ by using Eq. (9) for each $\rho\lambda^2$ value and we have repeated this procedure for 25 different point pattern realizations for each investigated structures. The circle markers and the error bars in Fig. 8(a) are the averaged values and the standard deviations corresponding to this ensemble-averaged operation, in the following identified by the symbol $\langle\cdots\rangle_e$. Specifically, all these curves cross the delocalization-localization threshold value $g = 1$ at the same optical density range, i.e., $\rho\lambda^2 \in [10^{-1}, 1]$, demonstrating the diffusion to localization transition.

To understand the observed transition in these structures, we must consider the ratio ξ/L, where L is the system size and ξ identifies the localization length provided by [72]

$$\xi \sim l_t \exp[\pi \Re(k_e) l_t/2], \tag{10}$$

with l_t the transport mean-free path and $\Re(k_e)$ the real part of the effective wave number in the medium. Although the numerical factor in Eq. (10) may not be accurate [72,73], it nevertheless tells us that the localization length in 2D systems is an exponential function of l_t and can be extremely large in the weak scattering regime (i.e., at low optical density). Specifically, for isotropic scattering systems discussed here, the transport mean-free path l_t coincides with the scattering mean-free path l_s, i.e., $l_t = 1/(\rho\sigma_d)$. Here, σ_d is the cross section of a single point scatterer, which is related to the 2D electric polarizability $\alpha(\omega)$ [60,61,64]. At resonance, σ_d is

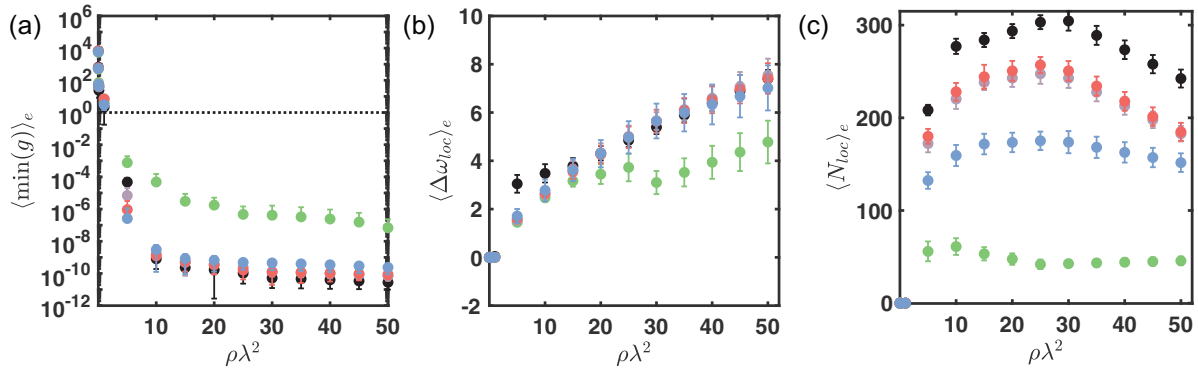

FIG. 8. (a) Trend of the minimum of the Thouless number as a function of $\rho\lambda^2$. (b) Width of the frequency range $\Delta\omega_{\text{loc}}$ for different optical densities where all the scattering resonances have a Thouless number lower than 1. (c) Number of localized scattering resonances as a function of $\rho\lambda^2$. All these parameters are averaged with respect to 25 different realizations and the error bars are the statistical errors associated with this average ensemble operation. The pastel green, violet, red, and blue markers refer to point patterns generated with a probability p equal to [1,1,1,0], [1,1,0.75,0.5], [1,0.75,0.75,0.5], and [1,0.75,0.5,0.25], respectively. The black markers denote the UR structure.

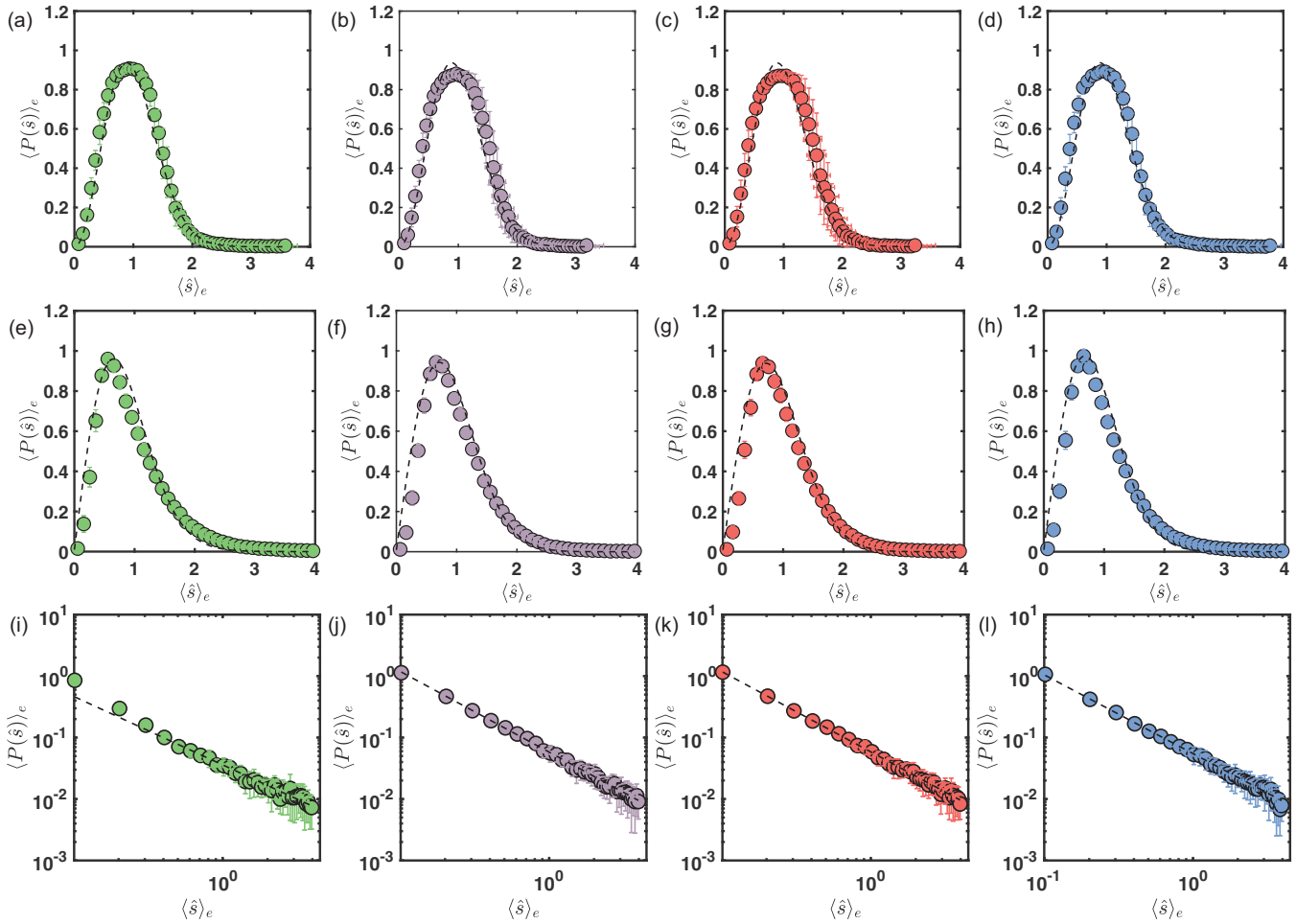

FIG. 9. Ensemble-averaged level-spacing distribution $P(\hat{s})$ as a function of the nearest-neighbor Euclidean distance of the complex eigenvalues $|\Delta\Lambda|=|\Lambda_{n+1}-\Lambda_n|$ normalized to their average value, i.e., $\hat{s}=|\Delta\Lambda|/\langle|\Delta\Lambda|\rangle$. (a)–(d), (e)–(h), and (i)–(l) correspond to a low (i.e., $\rho\lambda^2=10^{-6}$), intermediate (i.e., $\rho\lambda^2=10^{-1}$), and high (i.e., $\rho\lambda^2=50$) optical density regime, respectively. The black-dotted lines in (a)–(d), (e)–(h), and (i)–(l) identify the different statistics that better describe the evolution of $\langle P(\hat{s})\rangle_e$ by increasing $\rho\lambda^2$ (see the main text for more details). The pastel green, violet, red, and blue markers refer to point patterns generated with a probability p equal to [1,1,1,0], [1,1,0.75,0.5], [1,0.75,0.75,0.5], and [1,0.75,0.5,0.25], respectively.

equal to $k_0^3|\alpha(\omega_0)|^2/4$. Therefore, under the effective medium approximation, k_e can be expressed as $k_0+i/(2l_s)$ [60,61] and Eq. (10) can be rewritten as $\pi\lambda e^{2\pi^3\rho\lambda^2}/(2\rho\lambda^2)$, which relates the localization length of isotropic structures with their optical density. Using this estimate into Eq. (10), we found that the ratio of ξ/L is very large in the low optical density regime (i.e., $\rho\lambda^2=10^{-6}$), while it becomes smaller than one at larger optical density. This result is shown in Fig. 8(b), where the width of the frequency range $\Delta\omega_{\rm loc}$ corresponding to a Thouless number lower than 1 is reported for different optical densities. Moreover, Fig. 8(c) also displays the ensemble-averaged number of localized scattering resonances $\langle N_{\rm loc}\rangle_e$. Figure 8 clearly demonstrates that multifractal point patterns generated by multiplicative cascade processes localize scalar waves more efficiently than monofractal structures. Moreover, the data in Fig. 8(b) show a broader range of $\Delta\langle\omega_{\rm loc}\rangle$ for multifractals and URs compared to the monofractal structure (i.e., green-pastel markers). These results can be understood by considering the different structural properties of the investigated systems displayed in Fig. 4. Indeed, we observe that the multifractal structures with a radial distribution function that approaches unity, which from a structural view point are the most disordered of the multifractal systems, show localization properties more similar to the ones of uncorrelated disordered media [i.e., black markers in Fig. 8(a)]. Moreover, the multifractal structures with $g_2(r)$ that approaches the monofractal scaling of Fig. 4 display a progressively weaker localization behavior. Summarizing, the investigated systems are characterized by multiscale correlation properties that facilitate light localization of scalar waves and also support localized scattering resonances over broader frequency spectra akin to the ones predicted for uniform random systems.

To better understand the nature of localization in the investigated systems, we perform a statistical analysis of the level spacing distribution that is often utilized to identify different transport regimes in closed (Hermitian) and open systems [41,62,68,74]. In closed random systems, established results from random matrix theory predict the suppression of level repulsion in the presence of localized states [45]. In these systems, spatially isolated, exponentially localized modes hardly

influence each other and can coexist at energies that are infinitely close. The transition from diffusion to localization is confirmed by the switching from level repulsion to level clustering of the quantity $\langle P(\hat{s})\rangle_e$ as a function of $\rho\lambda^2$, which is demonstrated in Fig. 9. Here, $P(\hat{s})$ denotes the probability density function of the first-neighbor level spacing distribution of the complex eigenvalues of the Green s matrix [75]. It is well-established that the suppression of the level repulsion [i.e., $P(\hat{s}) \to 0$ when $\hat{s}$ goes to zero] indicates the transition into the localization regime for both scalar and vector waves in two-dimensional and three-dimensional disordered systems [74–76] as well as nonuniform aperiodic deterministic structures [39,62,71]. We found that $\rho\lambda^2 = 10^{-6}$, the distribution of the level spacing of the investigated arrays show excellent agreement with the GUE formula [45,77]:

$$P(\hat{s}) = \frac{32\,\hat{s}^2}{\pi^2}\, e^{-4\hat{s}^2/\pi}. \tag{11}$$

We emphasize that the black-dashed lines in Figs. 9(a)–9(d) are not the results of a numerical fitting procedure but are obtained by directly using Eq. (11). This distribution falls off quadratically for $\hat{s} \to 0$ [45,77], demonstrating that the eigenvalues of the investigated structures exhibit quadratic level repulsion in the low scattering density regime. Interestingly, the GUE distribution Eq. (11) has also been discovered in the characteristic spacing of the nontrivial zeros of the Riemann's zeta function [78], whose properties are intimately related to the distribution of prime numbers. Approaching the threshold of the discovered transition, the quantity $\langle P(\hat{s})\rangle_e$ manifests level repulsion described by the critical cumulative probability defined as [79]

$$I(s) = \exp[\mu - \sqrt{\mu^2 + (A_c s)^2}], \tag{12}$$

where μ and A_c are fitting parameters, as shown in Figs. 9(e)–9(h). The critical cumulative probability was successfully applied to describe the energy level spacing distribution of an Anderson Hamiltonian containing 10^6 lattice sites at the critical disorder value, i.e., at the metal-insulator threshold where it is known that all the wave functions exhibit multifractal scaling properties [79]. Our findings demonstrate the applicability of critical statistics to this class of multifractal structures reflecting the formation of critically localized eigenmodes with self-similar scaling properties.

In contrast, the level spacing distributions of all the investigated structures are well-reproduced by the inverse power law scaling curve $P(s) \sim s^{-\beta}$ [see black-dotted lines in Figs. 9(i)–9(l)] in the strong multiple scattering regime ($\rho\lambda^2 = 50$). In the context of random matrix theory, it has been demonstrated that the power-law distribution describes complex systems with multifractal spectra that produce uncountable sets of hierarchical level clustering [80,81]. Moreover, this power-law scaling is related to the phenomenon of anomalous diffusion. Anomalous diffusion is a transport regime in which the width of a wave packet σ^2 increases upon propagation according to $t^{2\nu}$ with $\nu \in [0, 1]$ [80]. Such a behavior was observed in different one- and two-dimensional aperiodic systems [81–83] and, more recently, in three-dimensional scattering arrays designed from subrandom sequences [71] and stealthy hyperuniform disordered systems [68]. The anomalous exponent ν is related to the parameter β through the relation $\nu = (\beta - 1)/d$ where d is the Euclidean dimension of the system [80,81]. By substituting the values of β obtained from the numerical fitting of the data in Figs. 9(i)–9(l), we find that the exponent ν is equal to 0.11 ± 0.03, 0.08 ± 0.01, 0.08 ± 0.01, and 0.06 ± 0.01 for structures generated with the probabilities vector p equal to [1,1,1,0], [1,1,0.75,0.5], [1,0.75,0.75,0.5], and [1,0.75,0.5,0.25], respectively. These values are very small and in fact approaching zero, which is consistent with the localization regime achieved at the largest optical density.

V. CONCLUSIONS

In conclusion, we have addressed the structural, spectral, and localization properties of multifractal arrays of electric point dipoles with different degrees of multiscale structural correlations. We systematically studied the multiple scattering properties of classical waves using the spectral Green's matrix method and demonstrated an enhanced localization behavior in multifractal structures compared to homogeneous fractals. In particular, we found strongly reduced Thouless numbers in the localization regime of multifractals accompanied by a larger number of localized scattering resonances with critical level spacing statistics at large optical density. Our results demonstrate the importance of tailoring multifractal correlations in the multiple scattering regime for the engineering of novel nanophotonic systems with broadband localization properties for optical sensing, lasing, and multispectral devices.

ACKNOWLEDGMENTS

L.D.N. acknowledges support from the National Science Foundation (No. ECCS-2110204).

APPENDIX A: MULTIFRACTAL ANALYSIS

Multifractal analysis is based on the scaling properties of the partition function $Z_q(\epsilon)$. We consider an object on which a measure μ is distributed with constant density so its multifractal properties are manifested purely in the scaling of its geometry. In this case, measure μ can be regarded simply as the mass density of the fractal object and the multifractal spectrum describes the geometrical support itself. The widespread box-counting method considers a uniform square grid of boxes with linear size ϵ and then introduces the local measure μ_i as the proportion of total mass of the object inside the ith box of size ϵ. Then the partition function is defined as

$$Z_q(\epsilon) = \sum_{i=1}^{N} \mu_i^q(\epsilon). \tag{A1}$$

The expression above denotes the sum of the qth moments of the local measures over all the boxes needed to cover the support and is also known as the moment sum. We note that the higher the values of q in Appendix A1, the more dense the selected regions.

Multifractal analysis assumes a power-law behavior for the partition function in the limit $\epsilon \to 0$ (or $N \to \infty$), and

therefore Eq. (A1) can be rewritten as

$$Z_q(\epsilon) \propto \epsilon^{(q-1)D_q}, \tag{A2}$$

where D_q is the spectrum of generalized dimensions. Note that the factor $q-1$ in the exponent ensures the validity of the normalization condition $Z_1(\epsilon)=1$. Inside each $\epsilon \times \epsilon$ box, the local contribution of the multifractal measure μ is assumed to scale according to

$$\mu_i \propto \epsilon^{\alpha_i}, \tag{A3}$$

where the local scaling exponent $\alpha_i = \alpha_i(\epsilon)$, also called the crowding index, is generally a position dependent quantity. Furthermore, the number of boxes with a given crowding index α can be expressed as

$$N_\alpha(\epsilon) \propto \epsilon^{-f(\alpha)}. \tag{A4}$$

Therefore, these boxes cover a subset with the fractal dimension $f(\alpha)$. At this point, we can immediately establish the following relation between the scaling function $\tau(q)$, the generalized dimension, and the partition function:

$$\tau(q) = (1-q)D_q = -\lim_{\epsilon\to 0}\frac{\log Z_q(\epsilon)}{\log \epsilon}. \tag{A5}$$

where log indicates the base 10 logarithm. Moreover, by using Eqs. (A3) and (A4), we see that the partition function satisfies

$$Z_q(\epsilon) \propto \int \epsilon^{\alpha q - f(\alpha)} d\alpha, \tag{A6}$$

where the integral above is slowly varying over the smallest scales. In the limit $\epsilon \to 0$, the integral above is dominated by the α values that minimize the exponent and it can be approximated using the saddle-point method. Therefore, when D_q and $f(\alpha)$ are differentiable functions we can obtain

$$f(\alpha) = \alpha q - (q-1)D_q, \tag{A7}$$

where α is given by

$$\alpha = \alpha(q) = \frac{d}{dq}[(q-1)D_q]. \tag{A8}$$

The results above show how the spectrum of generalized dimensions D_q (or τ_q) and the singularity (i.e., the multifractal) spectrum $f(\alpha)$ are connected by the Legendre transform and offer equivalent descriptions of the multifractal.

Finally, the generalized dimension D_q can be related to the partition function as follows:

$$D_q = \frac{1}{1-q}\lim_{\epsilon\to 0}\frac{\log Z_q(\epsilon)}{-\log\epsilon} = \frac{1}{1-q}\lim_{\epsilon\to 0}\frac{\log\sum_{i=1}^{N}\mu_i^q(\epsilon)}{-\log\epsilon}, \tag{A9}$$

where we recall that the local measure is the relative mass of the object in the ith box, i.e., $\mu_i = M_i(\epsilon)/M$ and M_i is the mass of the ith box and M is the total mass. For $q=0$, the expression above yields the box-counting dimension, for $q=1$ the information dimension, for $q=2$ the two-point correlation dimension. The generalized dimensions for $q>2$ provides information about higher-order correlations. For example, D_3 characterizes the correlations between triples of points in each box, D_4 between qaudruples, etc.

APPENDIX B: SINGLE SCATTERING PROPERTIES

The fractal dimension d_f of a structure can be obtained directly by measuring its correlation function, which is an observable quantity of fundamental importance in wave-scattering experiments (e.g., in light, x-ray, and neutron scattering) [52]. The density-density correlation function is defined as

$$g(\mathbf{r},\mathbf{r}') = \langle \rho(\mathbf{r})\rho(\mathbf{r}')\rangle, \tag{B1}$$

where $\rho(\mathbf{r})$ is the number density of atoms at position $\mathbf{r}$ and $\langle\ldots\rangle$ denotes an ensemble average. The expression above quantifies the correlations in the fluctuation of the number density. For isotropic atomic distributions, the correlation function depends on the radial distance $r = |\mathbf{r}-\mathbf{r}'|$, which is often defined in spherical coordinates. Additionally, for systems that display translational invariance on average (i.e., statistically homogeneous), we can fix $\mathbf{r}'=0$ and write

$$g(r) = \langle \rho(r)\rho(0)\rangle. \tag{B2}$$

We note that the $g(r)$ defined above, known as the pair correlation function, is proportional to the probability of finding a particle at a distance r from another particle of the system, which is proportional to the particle density $\rho(r)$ within a sphere of radius r. Since $\rho(r) = dM(r)/dV \propto r^{d_f-d}$ for a monofractal distribution, it follows that the correlation function scales as

$$G(r) \propto r^{d_f-d}, \tag{B3}$$

where d is the dimension of the embedding Euclidean space. The scattering intensity observed in actual experiments is proportional to the structure factor $S(q)$, which is essentially the Fourier transform of the pair correlation function:

$$S(q) = 1 + \frac{N}{V}\int_V [G(r)-1]e^{-i\mathbf{q}\cdot\mathbf{r}}d\mathbf{r}, \tag{B4}$$

where N is the total number of particles in the system of volume V and $q = \mathbf{k}-\mathbf{k}' = (4\pi/\lambda)\sin(\theta/2)$ is the momentum transfer. Note that the momentum transfer should not be confused with the parameter q used in the multifractal analysis. Here θ is the angle between the wave vectors $\mathbf{k}$ and $\mathbf{k}'$.

The scaling of the structure factor based on a pair distribution function with a generic power-law singularity $G(r) \propto r^{-\alpha}$ can be easily estimated by noting that

$$\begin{aligned} S(q) &\propto \int e^{-i\mathbf{q}\cdot\mathbf{r}} d^d r/r^\alpha = (q^\alpha/q^d)\int e^{-i\mathbf{q}\cdot\mathbf{r}}[d^d(qr)/(qr)^\alpha] \\ &\propto q^{\alpha-d}\int e^{-ix}x^{-\alpha}d^d x, \end{aligned} \tag{B5}$$

where $x = qr$. Remembering that in our case $-\alpha = d_f - d$, we immediately obtain

$$S(q) \propto q^{-d_f}. \tag{B6}$$

More sophisticated models for the structure factor of fractals that include finite-size effects have also been developed and are discussed in Refs. [56,57,84].

We now concisely address the role of structural correlations in the diffraction (single scattering) properties of multifractals. For simplicity, we consider a one-dimensional

measure $\mu(x)$ attached to some geometrical support of size L. We would like to evaluate the two-point correlations of the moments of $\mu(x)$ defined by

$$G_{mn}(y) = \langle \mu^m(x)\mu^n(x+y)\rangle_x \tag{B7}$$

where the brackets indicate averaging over all sites x and the correlation is between the local measures of boxes with fixed size ϵ and separation y. It has been shown in Ref. [85] that the correlation function of box measures can be described by exponents characterizing the multifractality of the set. In fact, due to the absence of characteristic length scales in the multifractal system, its pair correlation can be generally written as [27]

$$G_{mn}(y) \propto \epsilon^{x_1(m,n)} L^{-x_2(m,n)y} y^{x_3(m,n)}, \tag{B8}$$

where the new quantities x_1, x_2, x_3 must be related to the previously introduced multifractal exponents. This is obtained by computing the correlation between boxes separated by the box-size distances ϵ and L at which the boxes decorrelate. The steps of this derivation can be found in Ref. [27] where the following expression for $x_3(m, n)$ has been obtained:

$$x_3(m,n) = d_f - \tau(m) - \tau(n) + \tau(m+n), \tag{B9}$$

where $d_f = D_0$ is the fractal dimension of the support (Note the opposite sign convention for $\tau(q)$ used here compared to the one in Ref. [27]). Therefore, the pair correlation scales generally as [85]

$$G_{mn}(y) \propto y^{d_f - \tau(m) - \tau(n) + \tau(m+n)}, \tag{B10}$$

Thus, the measurement of spatial correlations can provide a quantitative test for multifractal behavior. Using the same argument that led to establish Eq. (B6), we can deduce the general scaling of the structure factor of a multifractal for given m and n values:

$$S_{mn}(q) \propto q^{-d_f + \tau(m) + \tau(n) - \tau(n+m)}. \tag{B11}$$

The relation above is quite important because it allows one to characterize the multifractality of a structure without box-counting procedures in numerical calculations, directly by studying the scaling of the structure factor for any given values of m and n. However, when spatial or angular averages are performed on scattering data, as in Fig. 4, the above formula cannot be directly applied and a more complex approach, beyond the scope of our paper, must be introduced.

[1] M. Berry, Diffractals, J. Phys. A: Math. Gen. **12**, 781 (1979).

[2] M. Soljacic, M. Segev, and C. R. Menyuk, Self-similarity and fractals in soliton-supporting systems, Phys. Rev. E **61**, R1048(R) (2000).

[3] M. A. Bandres, M. C. Rechtsman, and M. Segev, Topological Photonic Quasicrystals: Fractal Topological Spectrum and Protected Transport, Phys. Rev. X **6**, 011016 (2016).

[4] E. Aslan, E. Aslan, R. Wang, M. K. Hong, S. Erramilli, M. Turkmen, O. G. Saracoglu, and L. Dal Negro, Multispectral Cesaro-type fractal plasmonic nanoantennas, ACS Photonics **3**, 2102 (2016).

[5] L. Dal Negro and S. V. Boriskina, Deterministic aperiodic nanostructures for photonics and plasmonics applications, Laser Photonics Rev. **6**, 178 (2012).

[6] S. Torquato, Hyperuniform states of matter, Phys. Rep. **745**, 1 (2018).

[7] M. Segev, Y. Silberberg, and D. N. Christodoulides, Anderson localization of light, Nat. Photonics **7**, 197 (2013).

[8] J. D. Joannopoulos, P. R. Villeneuve, and S. Fan, Photonic crystals: Putting a new twist on light, Nature (London) **386**, 143 (1997).

[9] D. S. Wiersma, Disordered photonics, Nat. Photonics **7**, 188 (2013).

[10] A. Lagendijk, B. Van Tiggelen, and D. S. Wiersma, Fifty years of Anderson localization, Phys. Today **62**(8), 24 (2009).

[11] V. M. Shalaev, Optical negative-index metamaterials, Nat. Photonics **1**, 41 (2007).

[12] A. V. Kabashin, P. Evans, S. Pastkovsky, W. Hendren, G. A. Wurtz, R. Atkinson, R. Pollard, V. A. Podolskiy, and A. V. Zayats, Plasmonic nanorod metamaterials for biosensing, Nat. Mater. **8**, 867 (2009).

[13] N. I. Zheludev and Y. S. Kivshar, From metamaterials to metadevices, Nat. Mater. **11**, 917 (2012).

[14] P. Meakin, Fractal aggregates, Adv. Colloid Interface Sci. **28**, 249 (1987).

[15] J. Bibette, T. Mason, H. Gang, D. Weitz, and P. Poulin, Structure of adhesive emulsions, Langmuir **9**, 3352 (1993).

[16] C. Sorensen, Light scattering by fractal aggregates: A review, Aerosol Sci. Technol. **35**, 648 (2001).

[17] P. Barthelemy, J. Bertolotti, and D. S. Wiersma, A Lévy flight for light, Nature (London) **453**, 495 (2008).

[18] J. Bertolotti, K. Vynck, L. Pattelli, P. Barthelemy, S. Lepri, and D. S. Wiersma, Engineering disorder in superdiffusive Levy glasses, Adv. Funct. Mater. **20**, 965 (2010).

[19] H. G. E. Hentschel and I. Procaccia, The infinite number of generalized dimensions of fractals and strange attractors, Physica D **8**, 435 (1983).

[20] T. C. Halsey, M. H. Jensen, L. P. Kadanoff, I. Procaccia, and B. I. Shraiman, Fractal measures and their singularities: The characterization of strange sets, Phys. Rev. A **33**, 1141 (1986).

[21] M. Frame and A. Urry, *Fractal Worlds: Grown, Built, and Imagined* (Yale University Press, New Haven, CT, 2016).

[22] H. E. Stanley and P. Meakin, Multifractal phenomena in physics and chemistry, Nature (London) **335**, 405 (1988).

[23] B. B. Mandelbrot, in *An Introduction to Multifractal Distribution Functions, Fluctuations and Pattern Formation*, edited by H. E. Stanley and N. Ostrowsky (Kluwer, Dordrecht, 1988).

[24] A. Chhabra and R. V. Jensen, Direct Determination of the f(α) Singularity Spectrum, Phys. Rev. Lett. **62**, 1327 (1989).

[25] U. Frisch and G. Parisi, Fully developed turbulence and intermittency, Ann. N. Y. Acad. Sci. **357**, 359 (1980).

[26] B. B. Mandelbrot, Intermittent turbulence in self-similar cascades: Divergence of high moments and dimension of the carrier, J. Fluid Mech. **62**, 331 (1974).

[27] T. Nakayama and K. Yakubo, *Fractal Concepts in Condensed Matter Physics* (Springer Science & Business Media, New York, 2013), Vol. 140.

[28] Z.-Q. Jiang, W.-J. Xie, W.-X. Zhou, and D. Sornette, Multifractal analysis of financial markets: A review, Rep. Prog. Phys. **82**, 125901 (2019).

[29] R. H. Riedi, M. S. Crouse, V. J. Ribeiro, and R. G. Baraniuk, A multifractal wavelet model with application to network traffic, IEEE Trans. Inf. Theory **45**, 992 (1999).

[30] E. L. Albuquerque and M. G. Cottam, Theory of elementary excitations in quasiperiodic structures, Phys. Rep. **376**, 225 (2003).

[31] H. Sroor, D. Naidoo, S. W. Miller, J. Nelson, J. Courtial, and A. Forbes, Fractal light from lasers, Phys. Rev. A **99**, 013848 (2019).

[32] J. Trevino, S. F. Liew, H. Noh, H. Cao, and L. Dal Negro, Geometrical structure, multifractal spectra and localized optical modes of aperiodic Vogel spirals, Opt. Express **20**, 3015 (2012).

[33] A. Richardella, P. Roushan, S. Mack, B. Zhou, D. A. Huse, D. D. Awschalom, and A. Yazdani, Visualizing critical correlations near the metal-insulator transition in Ga1-x Mn x As, Science **327**, 665 (2010).

[34] A. Rodriguez, L. J. Vasquez, and R. A. Römer, Multifractal Analysis with the Probability Density Function at the Three-Dimensional Anderson Transition, Phys. Rev. Lett. **102**, 106406 (2009).

[35] M. Schreiber and H. Grussbach, Multifractal Wave Functions at the Anderson Transition, Phys. Rev. Lett. **67**, 607 (1991).

[36] F. Evers and A. D. Mirlin, Anderson transitions, Rev. Mod. Phys. **80**, 1355 (2008).

[37] K. Zhao, H. Lin, X. Xiao, W. Huang, W. Yao, M. Yan, Y. Xing, Q. Zhang, Z.-X. Li, S. Hoshino, *et al.*, Disorder-induced multifractal superconductivity in monolayer niobium dichalcogenides, Nat. Phys. **15**, 904 (2019).

[38] J. Chabé, G. Lemarié, B. Grémaud, D. Delande, P. Szriftgiser, and J. C. Garreau, Experimental Observation of the Anderson Metal-Insulator Transition with Atomic Matter Waves, Phys. Rev. Lett. **101**, 255702 (2008).

[39] R. Wang, F. A. Pinheiro, and L. Dal Negro, Spectral statistics and scattering resonances of complex primes arrays, Phys. Rev. B **97**, 024202 (2018).

[40] F. Sgrignuoli, Y. Chen, S. Gorsky, W. A. Britton, and L. Dal Negro, Optical rogue waves in multifractal photonic arrays, Phys. Rev. B **103**, 195403 (2021).

[41] F. Sgrignuoli, S. Gorsky, W. A. Britton, R. Zhang, F. Riboli, and L. Dal Negro, Multifractality of light in photonic arrays based on algebraic number theory, Commun. Phys. **3**, 106 (2020).

[42] L. Dal Negro, Y. Chen, S. Gorsky, and F. Sgrignuoli, Aperiodic bandgap structures for enhanced quantum two-photon sources, J. Opt. Soc. Am. B **38**, C94 (2021).

[43] L. Dal Negro, *Waves in Complex Media* (Cambridge University Press, Cambridge, UK, 2022).

[44] D. J. Thouless, Electrons in disordered systems and the theory of localization, Phys. Rep. **13**, 93 (1974).

[45] M. L. Mehta, *Random Matrices* (Academic Press, San Diego, 2004), Vol. 142.

[46] J.-F. Gouyet and A. L. Bug, Physics and fractal structures, Am. J. Phys. **65**, 676 (1997).

[47] K. Falconer, *Fractal Geometry: Mathematical Foundations and Applications* (John Wiley & Sons, West Sussex, UK, 2004).

[48] B. B. Mandelbrot, *The Fractal Geometry of Nature* (WH freeman, New York, 1982), Vol. 1.

[49] D. Harte, *Multifractals: Theory and Applications* (Chapman and Hall/CRC, CRC, Boca Raton, FL, 2001).

[50] V. J. Martinez, B. J. Jones, R. Dominguez-Tenreiro, and R. Weygaert, Clustering paradigms and multifractal measures, Astrophys. J. **357**, 50 (1990).

[51] B. B. Mandelbrot, Lognormal hypothesis and distribution of energy dissipation in intermittent turbulence, in *Multifractals and 1/f Noise* (Springer, New York, 1999), pp. 294–316.

[52] E. M. Anitas, *Small-Angle Scattering (Neutrons, X-Rays, Light) from Complex Systems: Fractal and Multifractal Models for Interpretation of Experimental Data* (Springer, Cham, Switzerland, 2019).

[53] S. Lovejoy and D. Schertzer, Scale invariance, symmetries, fractals, and stochastic simulations of atmospheric phenomena, Bull. Am. Meteorol. Soc. **67**, 21 (1986).

[54] S. Lovejoy, D. Schertzer, and A. Tsonis, Functional box-counting and multiple elliptical dimensions in rain, Science **235**, 1036 (1987).

[55] P. Meakin, Diffusion-limited aggregation on multifractal lattices: A model for fluid-fluid displacement in porous media, Phys. Rev. A **36**, 2833 (1987).

[56] T. Freltoft, J. K. Kjems, and S. K. Sinha, Power-law correlations and finite-size effects in silica particle aggregates studied by small-angle neutron scattering, Phys. Rev. B **33**, 269 (1986).

[57] P. Dimon, S. K. Sinha, D. A. Weitz, C. R. Safinya, G. S. Smith, W. A. Varady, and H. M. Lindsay, Structure of Aggregated Gold Colloids, Phys. Rev. Lett. **57**, 595 (1986).

[58] R. M. Soneira and P. Peebles, Is there evidence for a spatially homogeneous population of field galaxies? Astrophys. J. **211**, 1 (1977).

[59] M. Rusek and A. Orłowski, Analytical approach to localization of electromagnetic waves in two-dimensional random media, Phys. Rev. E **51**, R2763(R) (1995).

[60] A. Lagendijk and B. A. Van Tiggelen, Resonant multiple scattering of light, Phys. Rep. **270**, 143 (1996).

[61] O. Leseur, R. Pierrat, and R. Carminati, High-density hyperuniform materials can be transparent, Optica **3**, 763 (2016).

[62] F. Sgrignuoli, R. Wang, F. A. Pinheiro, and L. Dal Negro, Localization of scattering resonances in aperiodic Vogel spirals, Phys. Rev. B **99**, 104202 (2019).

[63] S. E. Skipetrov and I. M. Sokolov, Absence of Anderson Localization of Light in a Random Ensemble of Point Scatterers, Phys. Rev. Lett. **112**, 023905 (2014).

[64] F. Sgrignuoli and L. Dal Negro, Hyperuniformity and wave localization in pinwheel scattering arrays, Phys. Rev. B **103**, 224202 (2021).

[65] A. Cazé, R. Pierrat, and R. Carminati, Strong Coupling to Two-Dimensional Anderson Localized Modes, Phys. Rev. Lett. **111**, 053901 (2013).

[66] D. Bouchet and R. Carminati, Quantum dipole emitters in structured environments: A scattering approach: Tutorial, J. Opt. Soc. Am. A **36**, 186 (2019).

[67] F. Sgrignuoli, G. Mazzamuto, N. Caselli, F. Intonti, F. S. Cataliotti, M. Gurioli, and C. Toninelli, Necklace state hallmark in disordered 2D photonic systems, ACS Photonics **2**, 1636 (2015).

[68] F. Sgrignuoli, S. Torquato, and L. Dal Negro, Subdiffusive wave transport and weak localization transition in three-dimensional stealthy hyperuniform disordered systems, Phys. Rev. B **105**, 064204 (2022).

[69] E. Maciá, Physical nature of critical modes in Fibonacci quasicrystals, Phys. Rev. B **60**, 10032 (1999).

[70] C. S. Ryu, G. Y. Oh, and M. H. Lee, Extended and critical wave functions in a Thue-Morse chain, Phys. Rev. B **46**, 5162 (1992).

[71] F. Sgrignuoli and L. Dal Negro, Subdiffusive light transport in three-dimensional subrandom arrays, Phys. Rev. B **101**, 214204 (2020).

[72] P. Sheng, *Introduction to Wave Scattering, Localization and Mesoscopic Phenomena* (Springer Science & Business Media, Berlin, 2006), Vol. 88.

[73] B. C. Gupta and Z. Ye, Localization of classical waves in two-dimensional random media: A comparison between the analytic theory and exact numerical simulation, Phys. Rev. E **67**, 036606 (2003).

[74] S. E. Skipetrov and I. M. Sokolov, Magnetic-Field-Driven Localization of Light in a Cold-Atom Gas, Phys. Rev. Lett. **114**, 053902 (2015).

[75] J. M. Escalante and S. E. Skipetrov, Level spacing statistics for light in two-dimensional disordered photonic crystals, Sci. Rep. **8**, 11569 (2018).

[76] S. Mondal, R. Kumar, M. Kamp, and S. Mujumdar, Optical Thouless conductance and level-spacing statistics in two-dimensional Anderson localizing systems, Phys. Rev. B **100**, 060201(R) (2019).

[77] F. Haake, *Quantum Signatures of Chaos* (Springer Science & Business Media, Berlin, 2003).

[78] A. M. Odlyzko, On the distribution of spacings between zeros of the zeta function, Math. Comp. **48**, 273 (1987).

[79] I. K. Zharekeshev and B. Kramer, Asymptotics of Universal Probability of Neighboring Level Spacings at the Anderson Transition, Phys. Rev. Lett. **79**, 717 (1997).

[80] P. Cvitanovic, I. Percival, and A. Wirzba, *Quantum Chaos & Quantum Measurement* (Springer Science & Business Media, Berlin, 2013), Vol. 358.

[81] T. Geisel, R. Ketzmerick, and G. Petschel, New Class of Level Statistics in Quantum Systems with Unbounded Diffusion, Phys. Rev. Lett. **66**, 1651 (1991).

[82] I. Guarneri and G. Mantica, Multifractal Energy Spectra and Their Dynamical Implications, Phys. Rev. Lett. **73**, 3379 (1994).

[83] V. G. Benza and C. Sire, Band spectrum of the octagonal quasicrystal: Finite measure, gaps, and chaos, Phys. Rev. B **44**, 10343 (1991).

[84] A. Pearson and R. W. Anderson, Long-range pair correlation and its role in small-angle scattering from fractal clusters, Phys. Rev. B **48**, 5865 (1993).

[85] M. E. Cates and J. M. Deutsch, Spatial correlations in multifractals, Phys. Rev. A **35**, 4907(R) (1987).